Contact resistances in spark plasma sintering: From in-situ and ex-situ determinations to an extended model for the scale up of the process

Charles Manière, Lise Durand, Elodie Brisson, Henri Desplats, Patrick Carré, Philippe Rogeon, Claude Estournès

Contact resistances in spark plasma sintering: From in-situ and ex-situ determinations to an extended model for the scale up of the process

Charles Manière[a,b], Lise Durand[b], Elodie Brisson[c], Henri Desplats[c], Patrick Carré[c], Philippe Rogeon[c], Claude Estournès[a,*]

[a] CIRIMAT, Université de Toulouse, UMR 5085 CNRS – Université Toulouse III Paul-Sabatier – INPT, 118 Route de Narbonne, 31062 Toulouse Cedex 9, France
[b] CEMES, CNRS UPR 8011 and Université de Toulouse, 29 Rue Jeanne Marvig, 31055 Toulouse, France
[c] Université de Bretagne Sud, Centre de Recherche, LIMATB, F-56321 Lorient, France

A B S T R A C T

Heating in spark plasma sintering is a key point of this manufacturing process that requires advanced simulation to predict the thermal gradients present during the process and adjust them. Electric and thermal contact resistances have a prominent role in these gradients. Their determination is difficult as they vary with pressure and temperature. A calibration method is used to determine all of the contact resistances present within tools of different sizes. Ex situ measurements were also performed to validate the results of the in-situ calibrations. An extended predictive and scalable contacts model was developed and reveals the great importance and diversity of the contact resistances responsible for the general heating of the column and high thermal gradients between the parts. The ex/in situ comparison highlights a high lateral thermal contact resistance and the presence of a possible phenomenon of electric current facilitation across the lateral interface for the high temperatures.

Keywords:
Contact resistance
Spark plasma sintering
Graphite
Extended model
Joule heating

1. Introduction

The spark plasma sintering technique (SPS), also known as the field-assisted sintering technique (FAST), belongs to the hot pressing technologies, where a uniaxial pressure and a pulsed direct current is applied to the die. Over the past decade, SPS has been successfully used for a wide variety of materials in the main class [1,2] (metals and alloys, ceramics, polymers and composites). The general advantages of spark plasma sintering compared to traditional hot isostatic pressing or hot pressing, are [3,4] high heating rates, short processing time and the possibility to minimize grain growth known to improve the physical, optical or mechanical properties of materials, and the attainment of high densification [5].

The main difficulties of this technology are to control the temperature and densification field in the sample. The Finite Element Modeling (FEM) of the process is a solution to predict and adjust the internal physical parameters to the target objective. These simulations are developed on numerical codes containing: i) an electro-thermal (ET) component to predict the temperature field and ii) a mechanical component (M) to predict the powder densification. Most of the time, for the ET component pure resistive heating is considered without any inductive effects which is a good approximation of the phenomena [6–9]. These models are able to predict the behavior of the electric current (different depending on the electric conductivity of the sample), the area of high heat generation often located in the punches or the presence of hot spots. One of the most difficult phenomena to determine is the electric and thermal contact resistances (ECR and TCR) present at all the inner interfaces of the SPS column. These ECR and TCR result from non-ideal interfaces between the different parts with a certain roughness or from the presence of another material. Several authors have pointed out the importance and diversity of these contacts [10–13]. Anselmi-Tamburini et al. [14] suggested the punch/sample ECR is negligible for high pressure but pointed out the importance of the punch/die contact resistance. This last interface is very difficult to study because the lateral pressure governing a large part of the behavior of this contact is influenced by the thermal expansion of the punch, the gap in the punch/die interface and the possible compaction of the third material usually present at this interface (graphite foil, etc.). All of these parameters imply a very low contact pressure and are difficult to determine. For this reason, some authors chose to access the ECR and TCR by calibration of the temperature field [10,11,15,16] or by measurement of the overall column resistance in different configurations

* Corresponding author.
E-mail address: estournes@chimie.ups-tlse.fr (C. Estournès).

http://dx.doi.org/10.1016/j.jeurceramsoc.2016.12.010

Nomenclature

$\vec{J}$	Current density A m^{-2}	
$\vec{E}$	Electric field V m^{-1}	
κ	Thermal conductivity W m^{-1} K^{-1}	
σ	Electrical conductivity Ω^{-1} m^{-1}	
ρ	Density kg m^{-3}	
Cp	Specific heat capacity J kg^{-1} K^{-1}	
T	Temperature K	
σ_s	Stefan-Boltzmann's 5.6704.10^{-8} W m^{-2} K^{-4}	constant
ϕ_r	Radiative heat flux W m^{-2}	
ε	Emissivity 0.80 for graphite	
T_e	Emission surface temperature K	
T_a	Chamber wall temperature K	
ϕ_c	Conductive heat flux W m^{-2}	
$T_{inconel}$	Inconel wall temperature K	
T_w	Water temperature K	
h_c	Convective coefficient W m^{-2} K^{-1}	
J_c	Contact current density A m^{-2}	
$\dot{q}_c$	Contact heat flux W m^{-2}	
U_i (i equal 1 or 2)	Contact face electric potential V	
T_i (i equal 1 or 2)	Contact face temperature K	
ECR	Electric surface contact resistance Ω m^2	
TCR	Thermal surface contact resistance m^2 K/W	
θ	Porosity	
ρ_e	Electrical resistivity Ω m	
P	The contact pressure Pa	

[13,17]. These two in situ approaches have the advantage of quickly allowing the establishment of a heating model very close to experiment. But, the main drawback of these approaches is their domain of validity restrained to the experimental conditions of the model determination.

In order to approach a more generalized model of SPS heating, in this work we considered two approaches:

- in situ calibrations of the ECR and TCR for different geometries of the system 'punch, die, and sample' to extend the model and take into account the scaling effect.
- ex situ measurements of the ECR and TCR in different conditions of pressure and temperature to validate the in situ determinations and subsequently extend the model.

2. Experimental/computational methodology

2.1. SPS calibration experiments

All the in situ experiments for the calibrations were performed on the SPS machine (Dr. Sinter 2080, SPS Syntex Inc, Japan) of the Plateforme Nationale CNRS de Frittage Flash located at the University of Toulouse III-Paul Sabatier. The SPS column studied has six different types of contacts to be calibrated (Fig. 1). A graphite foil called papyex (® Mersen) is introduced at the punch/die, punch/sample and sample/die interfaces for easy removal of the sample and to ensure a good electrical contact. At the electrode/spacer interface, two graphite foils are introduced. The sample is 99.99% α-alumina powder (reference TM-DAR, Taimei Chemicals Co. Ltd, average initial grain size of 0.14 μm). For each test the rms value of the current delivered is measured by a Rogowki coil sensor (Power Electronic Measurements, CWT60) and temperatures are measured with K type thermocouples at different points of the SPS column.

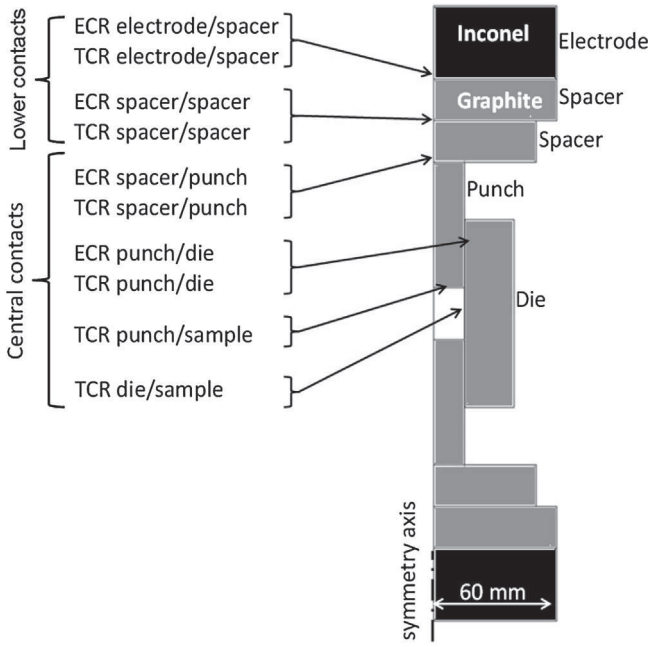

Fig. 1. Overview of the SPS column and the location of the ECR & TCR for the different inner contact interfaces.

Six calibration experiments were performed for in situ estimation of the ECR and TCR (Fig. 2). Three of them were devoted to the determination of the electrode/spacer and spacer/spacer contacts (also named lower contacts). All of these contacts are perpendicular to the applied load direction, then the resulting ECR and TCR can be related to the pressure exerted at each of these contacts. The geometrical configurations reported in Fig. 2a–c use simple graphite punches of 20, 30, 50 mm diameter placed between graphite spacers.

The three other experiments are devoted to the identification of the spacer/punch, punch/sample, sample/die and punch/die contacts (also named central contacts). The sample, die and punches geometries are reported in Fig. 2d–f are homothetically increased for punch diameters of 10, 20 and 30 mm. A constant pressure is applied during the whole cycle (including cooling), this allows verification of the TCR during the cooling step, a pure thermal stage of the cycle. A pressure of 100 MPa is applied for the calibration of the lower contacts. The aim of this high pressure is to minimize the TCR (punch/spacer) and it allows a strong heat flux to run through the lower contacts to be calibrated. The thermal cycle is a 100 K/min ramp up to 1000 °C and release of the current for the cooling stage.

Concerning the calibration of the central contacts, a constant pressure of 50 MPa is applied during the whole thermal cycle. This pressure is most useful for classical applications as it allows the densification of a wide range of materials without risk of die failure. The thermal cycle imposed at the die surface is the following: increase of the temperature from room temperature up to 1100 °C with a ramp of 100 K/min, a dwell of 1 min at 1100 °C and then the current is stopped for the cooling stage. For these configurations, the graphite felt that is classically added at the external die surface is not used here. This graphite felt decrease the die thermal radiative losses and then decrease the radial thermal gradient between the central column parts (punches, sample) and the edge of the die [12]. Even if this is beneficial for the sample homogeneity, for the calibration purpose, the impact of the vertical contact resistances on the temperature field is more distinguishable without the graphite felt. The higher is the ECR and TCR impact on the temperature field, the more accurate is the calibration of these ECR and TCR.

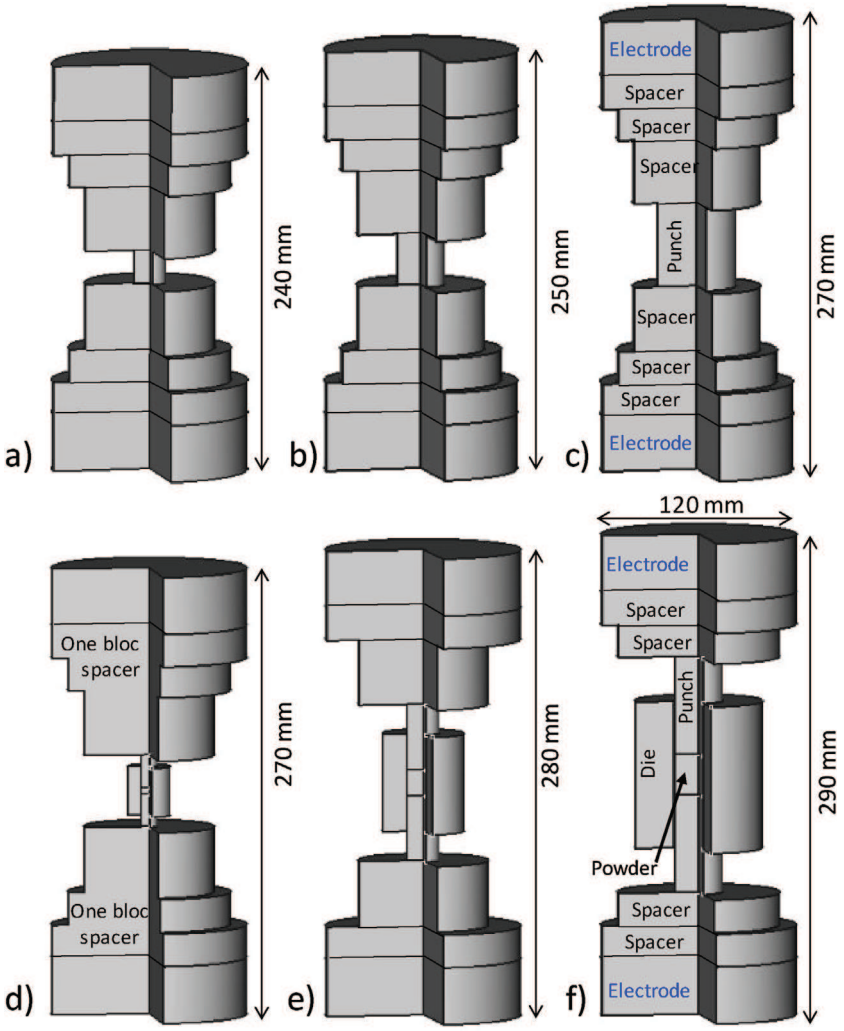

Fig. 2. Calibration test geometries.

2.2. The joule heating model

The Joule heating model obeys the current Eq. (1) and the heat Eq. (2):

$$\nabla \vec{J} = \nabla \left(\sigma \vec{E}\right) = 0 \tag{1}$$

$$\nabla \left(-\kappa \nabla T\right) + \rho C_p \frac{\partial T}{\partial t} = JE \tag{2}$$

The relevant physical properties of the different materials used for each part of the SPS column are given in Table 1.

The thermal model uses two main boundary conditions. Surface radiation obeys Eq. (3):

$$\phi_r = \sigma_s . \varepsilon . \left(T_e^4 - T_a^4\right) \tag{3}$$

The heat flux at the level of the water cooling system is governed by Eq. (4):

$$\phi_c = h_c . \left(T_{inconel} - T_w\right) \tag{4}$$

The electrical and thermal contact conditions at the inner interfaces obey Eqs. (5) and (6):

$$J_c = \frac{1}{ECR}\left(U_1 - U_2\right) \tag{5}$$

$$\dot{q}_c = \frac{1}{TCR}\left(T_1 - T_2\right) \tag{6}$$

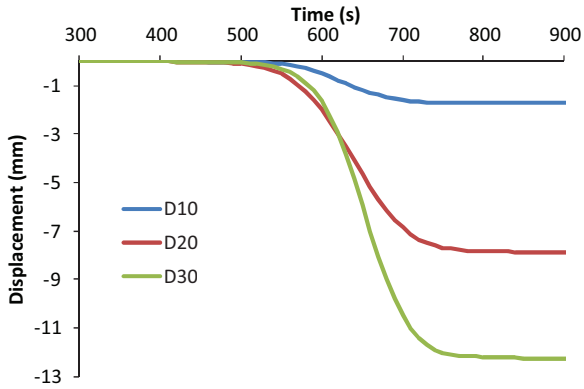

Fig. 3. Calculated displacement curves for the 10, 20 and 30 mm diameter experiments.

The shrinkage due to powder compaction is taken into account in the simulation by an Arbitrary Lagrangian Eulerian (ALE) moving mesh method. The shrinkage curves introduced into the model (Fig. 3) are calculated by an analytic Olevsky's model for sintering [18] previously determined for our alumina powder [19]. The

Table 1
Physical properties of inconel, graphite and alumina (with T in Kelvin).

Material	Heat capacity C_p ($J\,kg^{-1}\,K^{-1}$)	Thermal conductivity κ ($W\,m^{-1}\,K^{-1}$)	Electrical resistivity ρ_e ($\Omega\,m$)	Density ρ ($kg\,m^{-3}$)
Inconel	$344 + 2.50.10^{-1}\,T$	$10.1 + 1.57.10^{-2}\,T$	$9.82.10^{-7} + 1.6.10^{-10}\,T$	8430
Graphite	$34.27 + 2.72\,T - 9.60.10^{-4}\,T^2$	$123 - 6.99 \times 10^{-2}\,T + 1.55.10^{-5}\,T^2$	$1.70.10^{-5} - 1.87.10^{-8}\,T + 1.26.10^{-11}\,T^2 - 2.44.10^{-15}\,T^3$	$1904 - 0.01414\,T$
Alumina	850	$39\,500\,T^{-1.26}$	$8.70 \times 10^{19}\,T^{-4.82}$	3899

porosity dependence of the electro-thermal parameters is taken into account using the following approximated equations [2].

$$\rho_{e\ porous} = \rho_{e\ dense}\left(1 - \frac{3}{2}\theta\right)^{-1} \tag{7}$$

$$\kappa_{porous} = \kappa_{dense}\left(1 - \frac{3}{2}\theta\right) \tag{8}$$

$$C_{p\ porous} = C_{p\ dense}\left(1 - \theta\right) \tag{9}$$

2.3. The calibration methodology

We used, in this study, the calibration methodology employed in our two previous papers [15,16]. This methodology is a trial-and-error approach involving minimization of the experimental/simulated temperature field by the ECR and TCR calibration. In short, a first model not taking into account any ECR and TCR was applied and shows that the simulated temperatures are too low and homogeneous compared to the experimental ones. Then the ECR responsible for the overall increase of the temperatures and the TCR responsible for the main temperature differences between the parts are added, step by step, to the model and then adjusted until perfect accordance between the experimental and simulated temperatures is reached.

2.4. Ex situ ECR and TCR measurement methodology

2.4.1. ECR at the interface (graphite-papyex-graphite)

To determine the behavior of the ECR with both applied pressure and temperature an experimental design was used. The apparatus and method of measurement for the determination of ECR are described in details in Rogeon et al. [20].

The samples (two blocks of graphite separated by papyex foil) are placed in a power press (Instron 30 kN), between two stainless steel punches connected to a power supply (Hewlett Packard 6034A).

The two blocks of graphite, at the extremities of the stack, are connected with copper wires to a nanovoltmeter (Voltmetre Keithley 2002) allowing us to accurately measure the potential difference at the boundaries. The voltage taps are disposed at 1.5 mm from the ends of the graphite samples. The overall measurement of resistance R_{stack} is given by the ratio between the voltage and the current.

Two heating collars (power 600 W each) are fixed on the stainless steel punches. The heat flux crosses and heats the punches and the stack of samples by conduction. Two thermocouples (type K, diameter 0.1 mm) are introduced in each punch. The two thermocouples at the extremity of each punch allowed us to calculate the mean temperature of the sample stack. During the heating of the stack by conduction, the temperature can be assumed to be uniform inside the samples and at the interface between the samples. In the ex situ conditions, the contact temperature can be known. In contrast, during sintering, for the contact crossed by the electrical current, Joule heating occurs directly inside this interface, and the contact temperature rises sharply and cannot be measured accurately.

The stack is heated by conduction and the rise to 500 °C takes less than 20 min. During the temperature rise, the voltage at the extremities of the stack and the temperatures in the punches are recorded at a scanning frequency of 0.1 Hz. Under sintering conditions, the interfaces are subjected to higher heating rates. Indeed, the interfaces with the papyex between the punch and the die are crossed by a high current, and are heated directly by Joule effect. In this case the contact temperature inside the interface, between the graphite tools (die and punch) including the papyex, can rise faster than the temperature inside the tools in the vicinity of the interface. The overall resistance R_{stack} incorporates the two $ECR_{graphite/papyex}$, the resistance of the two samples in graphite ($R_{graphite}$), and the transverse electrical resistance of the papyex foil (R_{papyex}) (10).

$$R_{stack} = R_{graphite} + 2ECR_{graphite/papyex} + R_{papyex} \tag{10}$$

During the tests the thickness of the sheet of papyex could decrease and its transverse electrical conductivity could increase too. So it is not possible to correctly determine the variation of R_{papyex}. For this reason, only the resistance of the interface ($ECR_{graphite\text{-}papyex\text{-}graphite}$) including the resistance of the sheet of papyex (R_{papyex}) and the two $ECR_{graphite/papyex}$ can be estimated here (11).

$$ECR_{interface,\ papyex} = R_{papyex} + 2ECR_{graphite/papyex} = R_{stack} - R_{graphite} \tag{11}$$

$R_{graphite}$ is the bulk electrical resistance of the two graphite blocks calculated by using the electrical resistivity of the graphite (Table 1).

2.4.2. TCR at the two interfaces graphite-papyex-graphite and alumina-papyex-graphite

To determine thermal contact resistance, we use a method based on the same principle of sample stacking. The thermal contact resistances situated at the interfaces, between the alumina sample and the graphite die (including papyex foil) and also between two samples of graphite (including papyex foil) were measured with the specific ex situ device. The experimental setup (see block diagram in Fig. 4) used here is identical to that used by Rogeon et al. [20]. A detailed description of the setup can be found in Carre et al. [21]. Samples and tools are thermally instrumented with type K thermocouples. One-dimensional heat transfer was maintained by insulation placed around the stack to reduce lateral heat losses to the surroundings.

The heat flux crossing the stack is determined from measurements of temperatures using 8 thermocouples inserted respectively in the upper (T_0,T_1,T_2,T_3) and lower (T_4,T_5,T_6,T_7) copper punches. From the values given by these thermocouples, the average gradient temperature is calculated (Fig. 5). During the first stage, the temperature of the upper punch is raised to 300 °C. During the second stage, when stabilization of the temperatures is obtained in the two punches, the temperatures are recorded every ten seconds. The measurement range for the pressure is 5–20 MPa. The thermal resistance of the stack is determined knowing the mean heat flux crossing the stack and measured in the punches, and the temperature difference $\Delta T_{8\text{-}9}$ given by the two thermocouples 8 and 9 inserted into the samples at the extremities of the stack (Figs. 5 and 6). The thermal resistance of the stack is deduced using the relationship (12).

$$R_{stack} = \frac{\Delta T_{8-9}}{\kappa\left(\frac{dT}{dx}\right)_{average}} \tag{12}$$

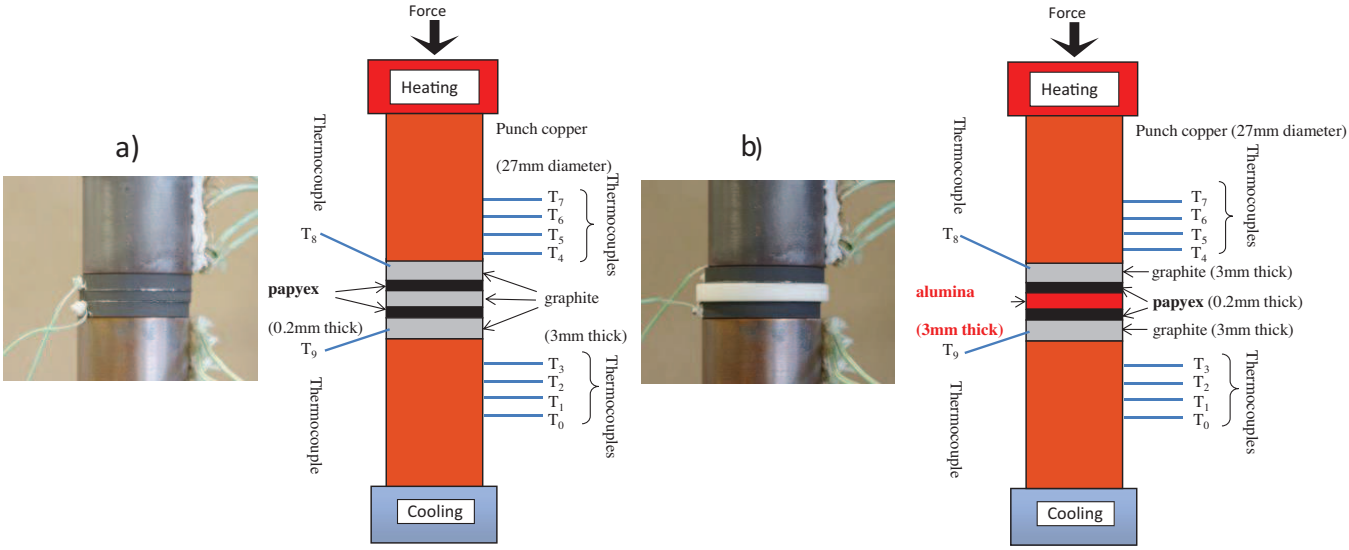

Fig. 4. Scheme of the thermal contact resistance measurement device for the two interfaces (with photograph of the two stacks): a) graphite-papyex-graphite, and b) graphite-papyex-alumina.

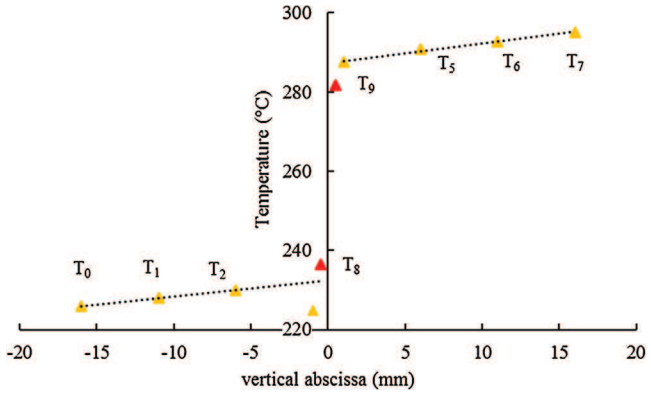

Fig. 5. Example of the spatial temperature distribution measured in the punches and in the samples at the extremities of the stack.

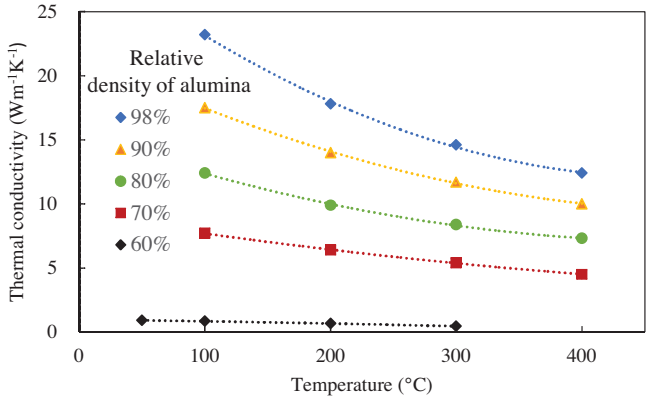

Fig. 6. Thermal conductivity of alumina versus temperature from green (60% relative density) to different sintered states (relative densities 70%, 80%, 90% and 98%). (For interpretation of the references to colour in this figure legend, the reader is referred to the web version of this article.)

2.4.2.1. TCR (graphite-papyex-graphite). The first stack (Fig. 4a) is composed of three graphite blocks separated from each other by papyex foil. The stack is placed between the two copper punches. Then the total thermal resistance of the stack is given by (13).

$$R_{th,\ stack} = R_{th,\ graphite} + 4TCR_{graphite/papyex} + 2\,R_{th,\ papyexs} \tag{13}$$

In Eq. (13), $R_{th,graphite}$ is the bulk thermal resistance of the three samples in graphite calculated by using the thermal conductivity given in Table 1.

For the same reasons as stated before, regarding the $ECR_{graphite\text{-}papyex\text{-}graphite}$, it is not possible to calculate the variation of the thermal resistance of the papyex foil. So, only the global interfacial resistance $TCR_{graphite\text{-}papyex\text{-}graphite}$, composed of two $TCR_{graphite\text{-}papyex}$ with one resistance of the papyex foil R_{papyex}, is reported here (14).

$$TCR_{graphite-papyex-graphite} = R_{th,papyex} + 2TCR_{graphite/papyex} = \frac{1}{2}(R_{th,stack} - R_{th,graphite}) \tag{14}$$

2.4.2.2. TCR(alumina- papyex-graphite). The second stack (Fig. 4b) is composed of an alumina sample placed between two blocks of graphite. The three samples are separated from each other by papyex foil. In the same way as for the previous stack, the total resistance of the new stack is determined following Eq. (15).

$$R_{th,\ stack} = R_{th,\ graphite} + R_{th,\ alumina} + 2TCR_{papyex/graphite} + 2TCR_{papyex/alumina} \tag{15}$$

The global thermal contact resistance of the interface, between alumina and graphite $TCR_{alumina\text{-}papyex\text{-}graphite}$ integrating the papyex foil resistance, can be calculated from Eq. (16) derived from relation (15).

$$TCR_{alumina-papyex-graphite} = TCR_{papyex/alumina} + R_{th,\ papyex} + TCR_{papyex/graphite} = \frac{1}{2}(R_{th,\ stack} - R_{th,\ graphite} - R_{th,\ alumina}) \tag{16}$$

The tests have been carried out using sintered samples of alumina with the highest relative density (98%) and having the lowest thermal conductivity, to decrease the bulk resistance of the materials in the stack as much as possible (Fig. 6). Thermal conductivity was deduced from the measurements of the diffusivity using a Netzsch LFA 457 diffusivimeter, based on the flash method.

3. Results and discussion

Paragraphs 3.1–3.3 are devoted to the SPS in situ determination of the ECR and TCR. Paragraphs 3.4 and 3.5 are devoted to ex situ

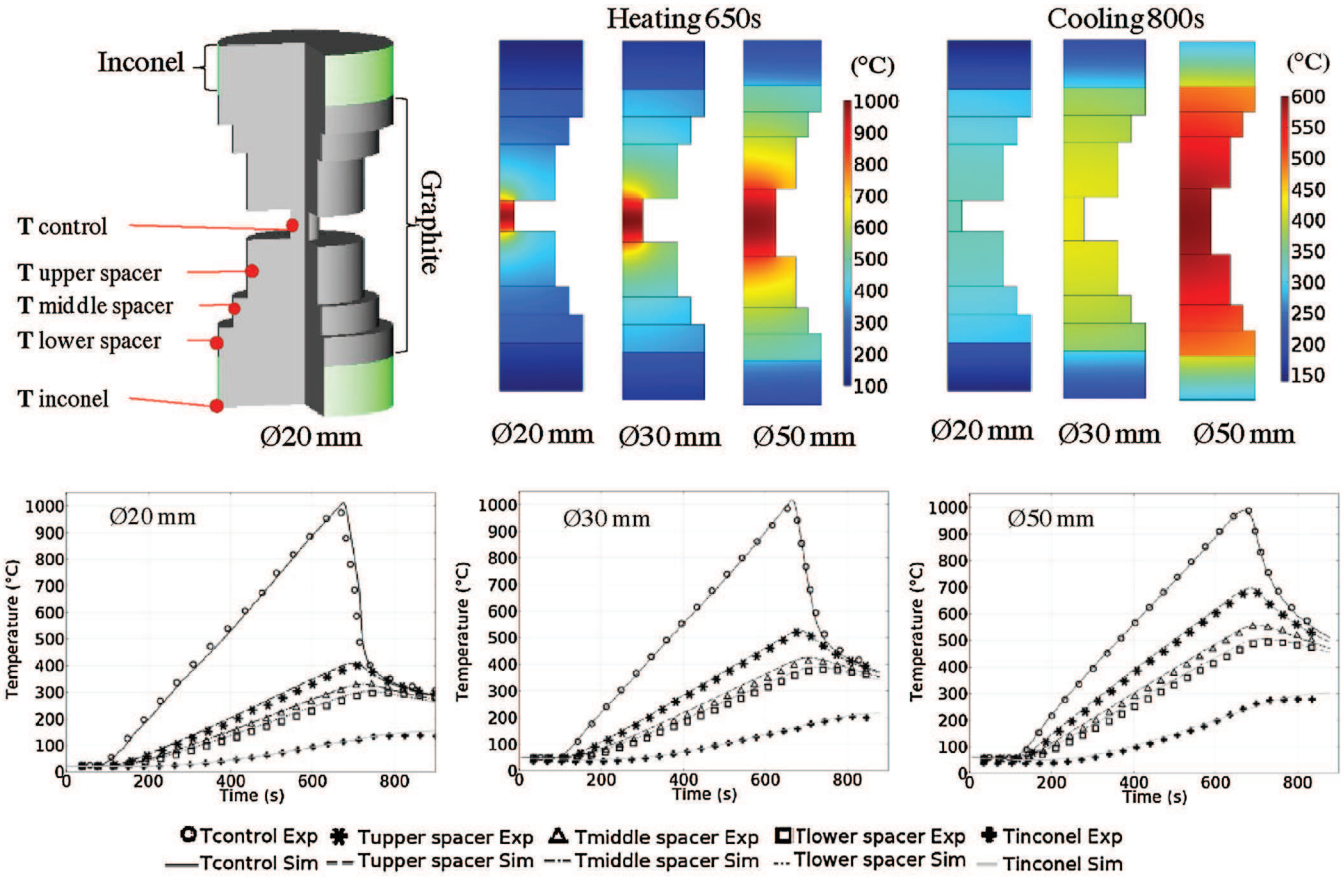

Fig. 7. Post-calibrated temperature results for the lower contact model: (upper) vertical section of the modelled temperature field during the heating and cooling stage, (lower) Experimental/simulated temperature curves.

ECR and TCR measurement. Both types of results obtained from in situ and ex situ measurements are then discussed.

3.1. Electrode/spacer and spacer/spacer contact calibration

The calibrated model for the lower contacts is reported in Fig. 7. The punch/spacer ECR and TCR are 1E–9 Ωm^2 and 1E–5 m^2 K/W for a pressure of 100 MPa and a temperature up to 850 °C. These values are very low and could be ignored as their addition only modifies in the calibration by a few degrees. The ECR and TCR spacer/spacer (graphite/graphite) and electrode/spacer (inconel/2Xpapyex/graphite) are reported Fig. 8 with the corresponding interface pressure. These contact resistances have a greater effect, especially the inconel/2Xpapyex/graphite which is responsible for a temperature gap of up to 100 K between the electrode and spacer (Fig. 7). These ECR and TCR are of the order of magnitude of 1E–7 $\Omega\,m^2$ and 1E–3 m^2 K/W for the inconel/2Xpapyex/graphite contacts and 1E–9 $\Omega\,m^2$ and 1E–5 m^2 K/W for the graphite/graphite contacts. The electrode/spacer contact resistances are considerably higher than the spacer/spacer contact resistances. The high TCR value at the electrode/spacer contact protects the electrode from the elevated temperatures inside the graphite column. The value of the convective coefficient h_c can be estimated with the electrode temperature and is about 200 $W\,m^{-2}\,K^{-1}$.

The ECR and TCR are expected to decrease with the temperature and the pressure; but in the configurations in Fig. 2a–c, the assumption of constant values is reasonable to describe the thermal phenomena. For the following central contact calibration (Fig. 2d–f), the decrease of the ECR and TCR with temperature is required.

3.2. Spacer/punch, punch/sample, sample/die and punch/die calibration

In order to calibrate the central ECR and TCR (Fig. 2d–f), five thermocouples are placed in different locations as reported in Fig. 9. Four thermocouples are placed in the different parts, respectively in the punch, the sample, the papyex, and the last one is fixed to the nearest electrode spacer. The last one is the control thermocouple placed at the die surface. The post-calibration temperature fields results are reported Fig. 9 with, on the upper part, the heating and cooling temperature fields respectively at 700 s and 900 s, and on the lower part, the comparison between experimental versus simulated curves after the calibration. During the heating stage, the temperature seems to be higher in the punch compared to the die. This effect is increased in the last configuration with the 30 mm diameter punch, with the appearance of a high hot spot inside the punch. For this experiment, the spacer volume is the lowest of the three tests. Consequently, the punch outlet heat is more difficultly evacuated by the spacer volume in the 30 mm punch diameter test. Moreover, the high TCR of the electrode/spacer interface, which in this case is closer to the punch, slows down the outlet heat flux through the cooling elements; this is one explanations of the spacer temperature increase with the punch diameter. The higher accumulation of heat in the punches can be explained by the combination of two phenomena: a high punch/die TCR responsible for a high temperature difference between the punch and the die con-

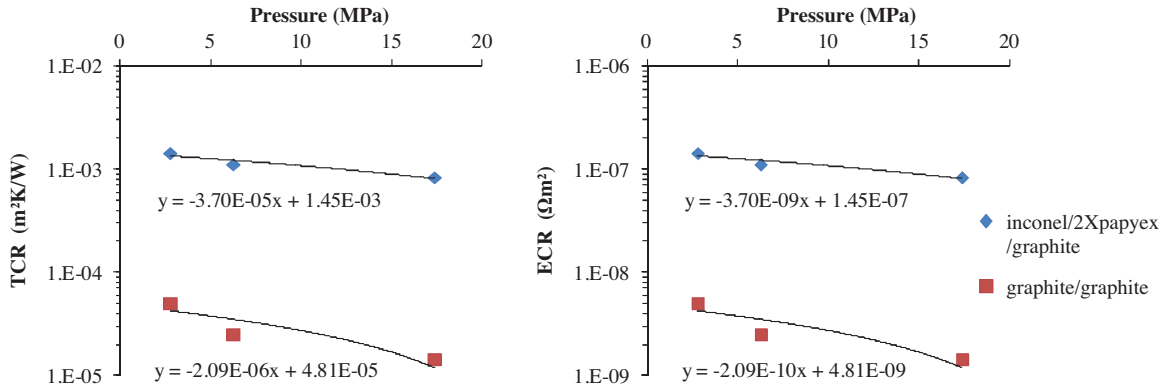

Fig. 8. TCR (left) and ECR (right) values for the lower contacts for each interface pressure.

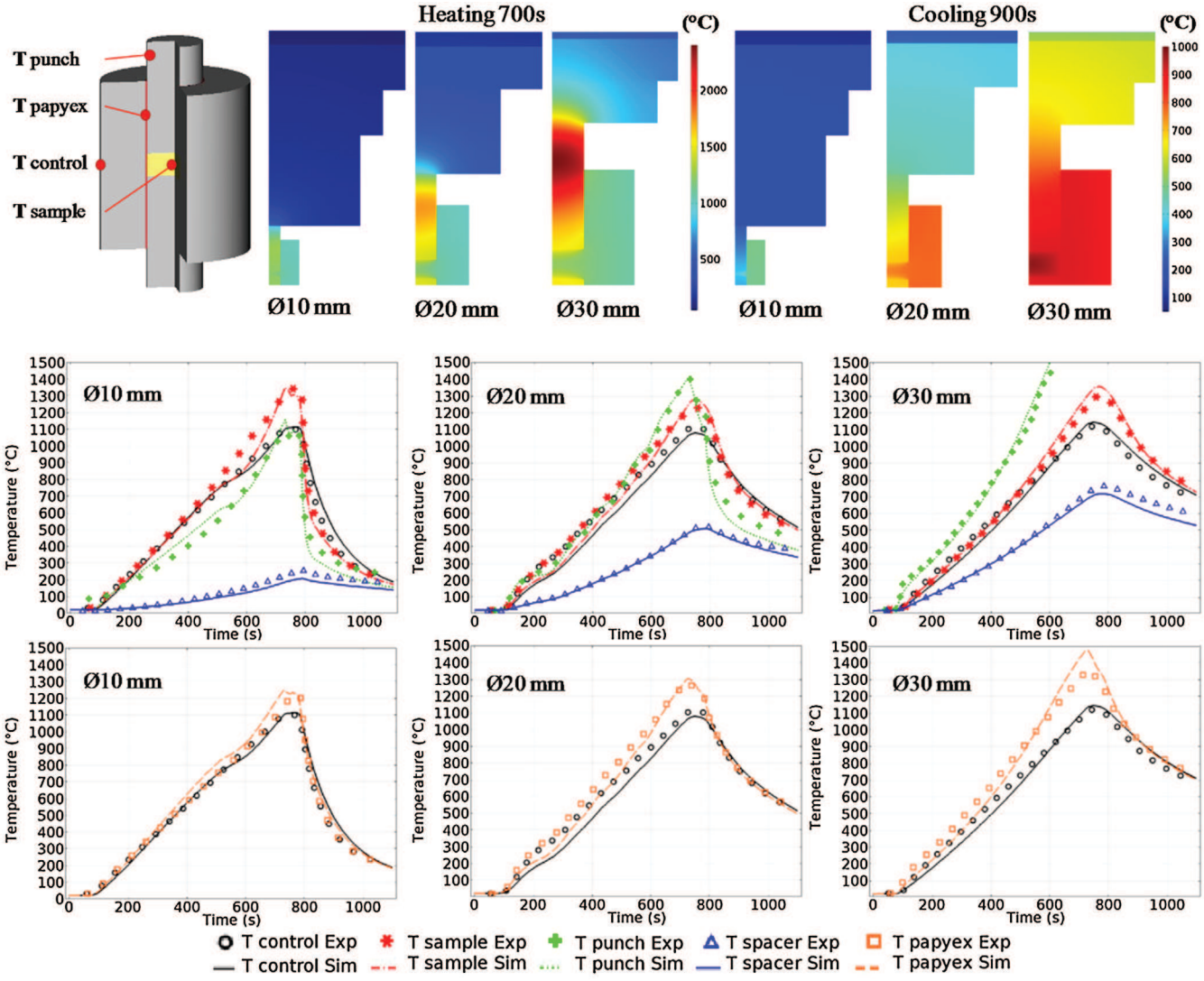

Fig. 9. Post-calibrated temperature results for the central contact model: (upper) vertical section of the modelled temperature field during the heating and cooling stage, (lower) Experimental/simulated temperature curves.

trol thermocouple, and the minimization of the punch outlet heat by reduction of the spacer volume.

During the cooling stage the temperature is higher in the die compared to the rest of the SPS column. In both heating and cooling regimes the high punch/die TCR implies a high temperature difference between the punches and the die. This temperature difference can be optically observed for the 30 mm punch diameter test reported in Fig. 10. The punch/die TCR is then one of the most important parameters to take into account to have a realistic simulation of the temperature field. Another interesting point is the sample temperature field. The thermal conductivity of the alumina is lower than that of the graphite. During the heating stage, as

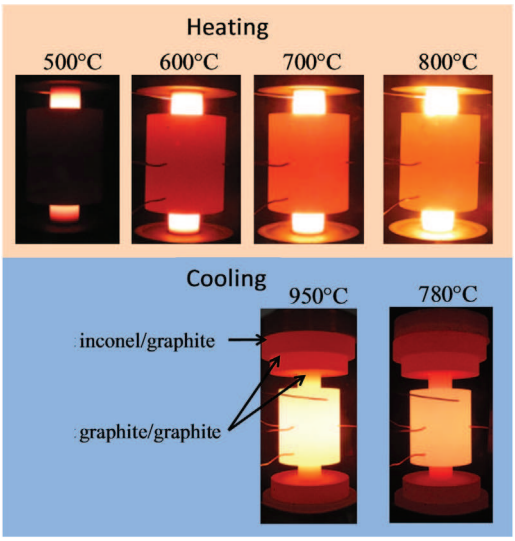

Fig. 10. Picture of the 30 mm diameter experiment at different stages of the cycle (indicated temperatures are located at the die surface).

Table 2
ECR and TCR electrode/spacer and spacer/spacer.

	10 mm diameter	20 mm diameter	30 mm diameter
ECR electrode/spacer ($\Omega\,m^2$)	3.33E-7	2.50E-7	8.33E-8
TCR electrode/spacer (m^2 K/W)	3.33E-3	2.50E-3	8.33E-4
ECR spacer/spacer ($\Omega\,m^2$)	One bloc spacer	5.00E-9	2.00E-9
TCR spacer/spacer (m^2 K/W)	One bloc spacer	5.00E-5	2.00E-5

shown in Fig. 10, the areas of highest temperature are located in the punches, thus the higher temperature zone of the sample can be considered near the punches while during the cooling stage, due to the TCR and the thermal conductivity values of alumina and graphite, one can consider that the maximum temperature zone of the sample can be situated in its center.

The calibrated ECR and TCR for the electrode/spacer and spacer/spacer (of experiments Fig. 2d–f) are reported in Table 2. The ECR and TCR spacer/punch are submitted to a constant pressure of 50 MPa but the contact temperature variation is high. In the simulation, the variation of the contact resistances with time is determined step by step. The post-calibration ECR(t) and TCR(t) are then reported versus the evolution of the average contact temperature simulated in Fig. 11 (upper graphs). The interface temperature changes are determined post-simulation by the average temperature of the two interfaces. The ECR punch/sample and sample/die are ignored because the alumina is an electric insulator, but the TCR are considered (Fig. 11 middle graphs).

The punch/die and sample/die interfaces are more complex, and play a major role in the heating process of the sample. Indeed, the electrical current should get round the alumina sample by crossing the two interfaces punch/die. In a previous paper [15], we show the current density is locally very high in the area near the punch outlet and induces at this place a strong heat generation by Joule effect. We also showed that a non-negligible quantity of this heat is maintained in the papyex thickness because of the presence of high $TCR_{papyex/punch}$ and $TCR_{papyex/die}$ and this heat can diffuse along the papyex to the sample. Moreover, the papyex foil located at the punch/die interfaces is subjected to a lateral pressure due to the thermal expansion of the punch (hotter than the die) and Poisson deformation. This pressure is expected to have a high variation with the temperature and a very low value because of the 0.2 mm punch/die gap where the 0.18 mm thick (after rolling)

Table 3
Fitted expressions of the ECR and TCR spacer/punch, punch/sample and punch/die.

ECR spacer/punch ($\Omega\,m^2$)	$5*10^{-9}\frac{(2000-T)}{(T-100)}$
TCR spacer/punch (m^2 K/W)	$5*10^{-6}+3*10^{-5}\frac{(2000-T)}{(T-50)}$
TCR punch/sample (m^2 K/W)	$2.5*10^{-5}+1.5*10^{-5}\frac{(2000-T)}{(T-50)}$
TCR sample/die (m^2 K/W)	$8*10^{-6}+4*10^{-6}\frac{(2000-T)}{(T-80)}$
ρ_{ex} (punch/die) (Ω m)	$\left(1.7*10^{-3}-9.5*10^{-7}*T\right)*F_e$
ρ_T (punch/die) (K m/W)	$\left(80+50\frac{(2000-T)}{(T-80)}\right)*F_T$

compressible graphite foil is introduced. For instance, this contact pressure remains unknown because of the unknown compressibility behavior of the graphite foil. This contact pressure is also strongly influenced by the initial punch/die gap. The machining precision and/or the possible tool distortions after repeated uses of this gap interface is then an important point. If this gap dimension is not enough controlled, this can lead to highly non-reproducible thermal responses. Indeed, the punch/die TCR has a great impact on the die-sample temperature difference and is strongly impacted by the punch/die interface pressure. The punch/die ECR and TCR, in the transversal direction, are equal to the addition of the electrical resistance of the papyex foil with the two contact resistances punch/papyex and papyex/die (17–18).

$$ECR_{punch\text{-}die} = ECR_{punch\text{-}papyex} + ECR_{papyex\text{-}die} + RE_{papyex}\,(\mathrm{Ohm\,m^2}) \quad (17)$$

$$TCR_{punch\text{-}die} = TCR_{punch\text{-}papyex} + TCR_{papyex\text{-}die} + RT_{papyex}\,(\mathrm{K\,m^2/W}) \quad (18)$$

The punch/die ECR and TCR are modelled with the approach described in a previous paper [15]. The punch/die ECR is globally modelled here by a resistive layer with an anisotropic effective electrical resistivity ρ_e (ρ_{ex}, ρ_{ey}) of thickness 0.2 mm, corresponding to the initial punch/die gap where the papyex is introduced, which is assumed constant (19).

$$\rho_{ey} = \rho_{egraphite}(\text{Table1})ECR_{punch\text{-}die} = 0.2\text{E-}3{*}\rho_{ex}(\Omega\,m^2) \quad (19)$$

ρ_{ex} (Table 3) includes the added effects of the two contact resistances $ECR_{punch\text{-}papyex}$ and $ECR_{papyex\text{-}die}$, and of the unknown variation of the electrical resistance of the papyex compressive foil RE_{papyex}.

Concerning the punch/die interface, unlike the electrical effects of the ECRs and of the papyex foil which have been considered globally in a contact layer, the thermal effects of the TCRs and of the papyex foil should be considered separately in the contact model. The punch/die TCR is modelled by a constant thickness (0.2 mm) resistive layer with anisotropic effective thermal conductivity κ (κ_x, κ_y), surrounded by the two TCRs punch/papyex and papyex/die (20). The two TCRs are here assumed to be identical, and are modelled by a virtual thermal resistive layer of 0.1 mm thickness and of thermal resistivity ρ_T (21).

$$TCR_{punch\text{-}die} = TCR_{punch\text{-}papyex} + TCR_{papyex\text{-}die} + 0.2\text{E-}3/\kappa_x\,(\mathrm{K\,m^2/W}) \quad (20)$$

$$TCR_{punch\text{-}die} = 2{*}(0.1\text{E-}3{*}\rho_T) + 0.2\text{E-}3/\kappa_x\,(\mathrm{K\,m^2/W}) \quad (21)$$

The value of ρ_T includes the global effects of the $TCR_{punch/papyex}$ and of $TCR_{papyex/die}$ and the unknown variation of the thermal resistance of the papyex compressive foil. In a previous study [15], this specific modelling of the punch/die TCR allowed us to achieve by the simulation a good predictability of some observed experimental phenomena such as the papyex local overheating and the appearance of a hot spot near the sample for small sample thicknesses. The equivalent thermal conductivity of the anisotropic interfacial layer in the normal and plane directions (κ_x, κ_y) are given by Eq. (22).

$$\kappa_x = \kappa_{graphite}(\text{Table1}),\ \kappa_y = 10{*}123 - 6.99\text{E-}2T + 1.55\text{E-}5T^2\,(\mathrm{W\,m^{-1}\,K^{-1}}) \quad (22)$$

The ρ_e and ρ_T values are reported in Fig. 11 (lower graphs) and the expression form of the fit curves are given by Eqs. (23) and (24):

$$\rho_e = (aT+b)*Fe\ \Omega\mathrm{m} \quad (23)$$

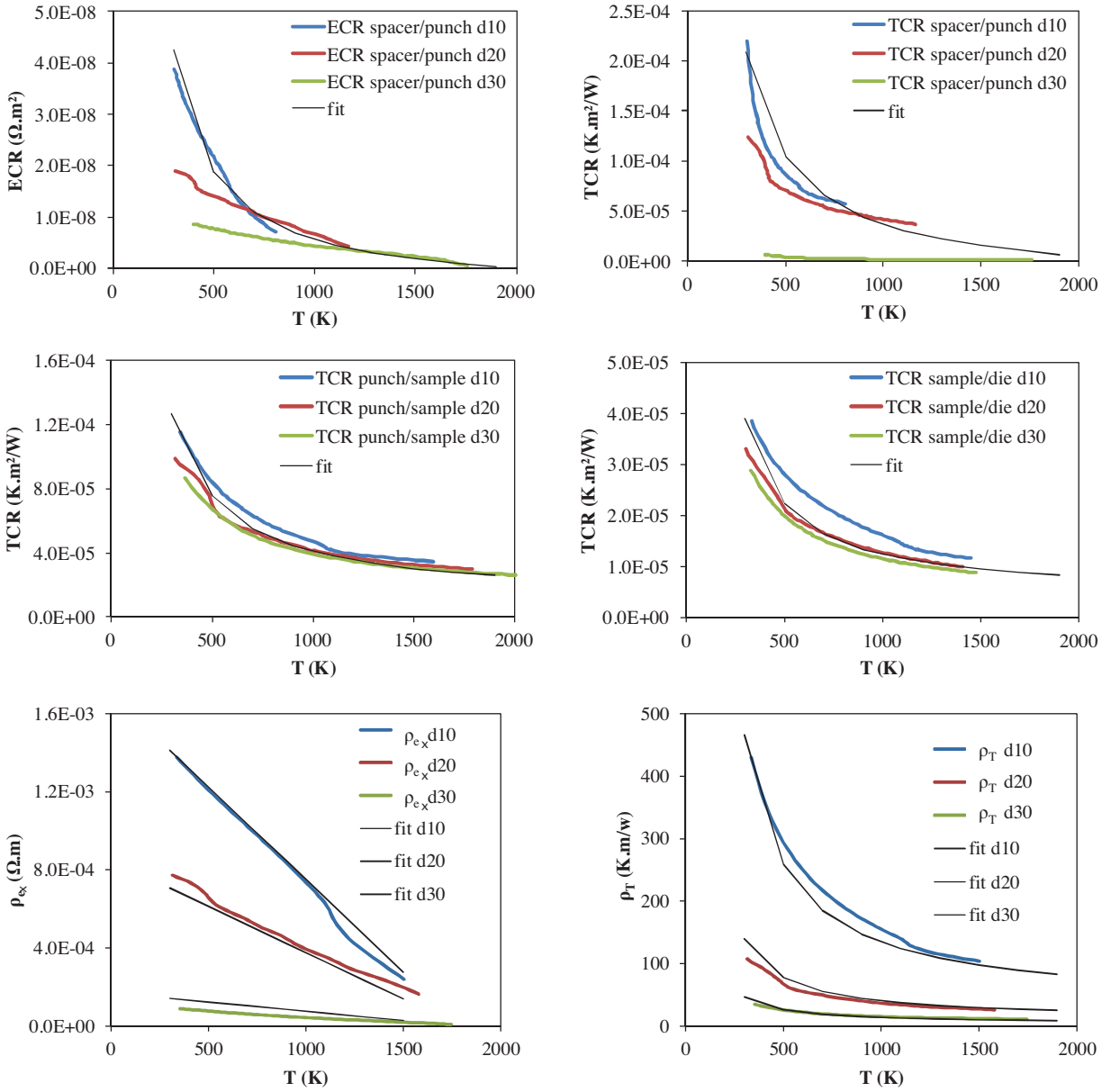

Fig. 11. Calibrated ECR and TCR for each of the central contacts.

With, a and b constant values, T the absolute temperature and *Fe* a dimension dependent factor.

$$\rho_T = \left(c + d\left(\frac{g-T}{T-h}\right)\right) * F_T \ \mathrm{KmW^{-1}} \tag{24}$$

With, c, d, g and h constant values, T the absolute temperature and F_T a dimension dependent factor.

More than for the other contacts, the identified values of ρ_e and ρ_T for the three diameters tested show pronounced discrepancies, probably because of the differences in contact pressure. Because the lateral contact pressure is for instance impossible to determine in a phenomenological approach the variation of the punch/die ECR and TCR are directly related to the punch diameter by the *Fe* and the F_T parameters reported in Fig. 12. The fit equations of the central contacts are reported in Table 3.

3.3. *Verification test*

The extended contact model is identified for 50 MPa and diameters between 10 and 30 mm. This model is tested with an independent 15 mm diameter test. The geometrical configuration is reported in Fig. 13a where five thermocouples have been used to compare the simulated/experimental temperatures. Further, the geometry of the die used for this test is not homothetic to the ones used for the identification configurations (Fig. 2d–f) but the nature of the materials and interfaces are the same. This will support the validity of the modelled contact resistances obtained if the comparison simulation/experimental results is consistent. The thermal cycle is a simple temperature ramp from room temperature up to 1100 °C at a rate of 100 K/min and then the current is stopped immediately for the cooling stage. The ECR and TCR previously identified are introduced into all the contact interfaces. The simulated temperature map (obtained at the middle of the die) at the end of the heating step is reported in Fig. 13b with a photograph of the

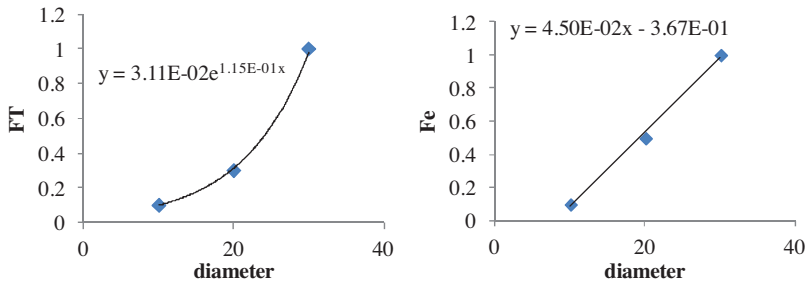

Fig. 12. Diameter dependence of the Fe and FT fit factors.

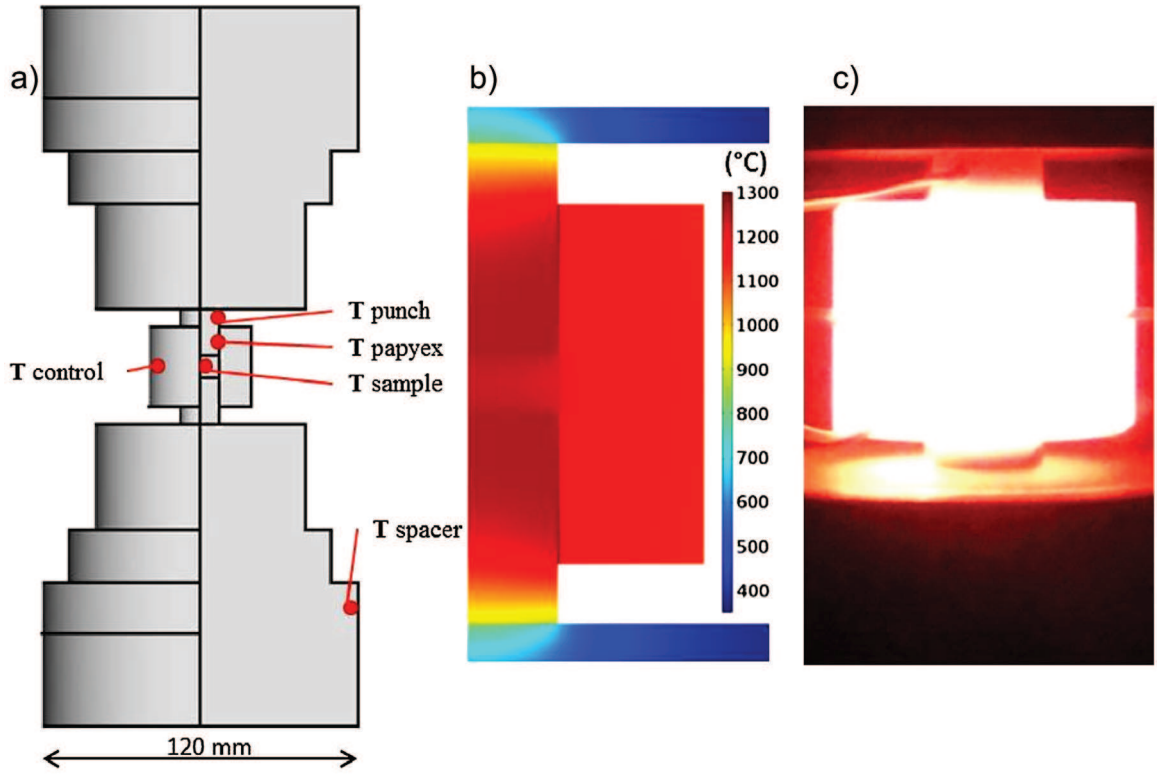

Fig. 13. Independent verification experiment: a) geometrical configuration, b) temperature field at 700s, c) picture of the experiment during the heating stage (different colour scale).

die taken at the same time in Fig. 13c. The temperature distribution observed during the heating is close to the calibration Fig. 9. The punches have a higher temperature compared to the die and a marked punch/die temperature gap is observed with concentration of heat in the graphite foil. The overall temperature field obtained (Fig. 13c) is in good agreement with the temperature field obtained by the simulation (Fig. 13b), as evidenced by the temperature at the periphery of the punch near the die which is close to the die temperature and decreases along it on the direction of the punch/spacer interface.

The experimental/calculated temperatures are reported in Fig. 14 for the simulations with and without the ECR and TCR previously determined in the extended model. The temperature confrontation shows a very good agreement between the experimental/simulated temperatures, the maximum temperature differences are about 50 K or less. This is an interesting result considering that we introduced the ECR and TCR values calibrated for different configurations. On the other hand, the simulation without ECR and TCR shows, as expected, very poor results with temperature differences of 400 K. This result points out the crucial importance of the ECR and TCR to attain more realistic simulations for SPS heating.

3.4. *Ex situ measurements*

We report the outcome measurements concerning the $ECR_{graphite\text{-}papyex\text{-}graphite}$ evolutions versus pressure and versus temperature (Fig. 15a and b). At room temperature, when the pressure increases in the range [2 − 15 MPa], the $ECR_{graphite\text{-}papyex\text{-}graphite}$ is reduced by about a factor of 2. At room temperature the evolution of the $ECR_{graphite\text{-}papyex\text{-}graphite}$ according to the pressure P in MPa, can be modelled by a power law (25).

$$ECR_{interface,papyex} = 2.77E{-}7\,P^{-0.264} \quad (25)$$

The effect of a temperature, increased from ambient temperature 295 K up to 730 K, is a decrease of $ECR_{interface,papyex}$ from 2.6E-7 to 1.4E−7 Ω m^2, for a 15 MPa pressure applied on the stack.

The ex situ measurements of TCR were achieved for graphite-papyex-graphite and alumina- papyex-graphite interfaces. The measurements were made at a mean temperature of 250 °C versus

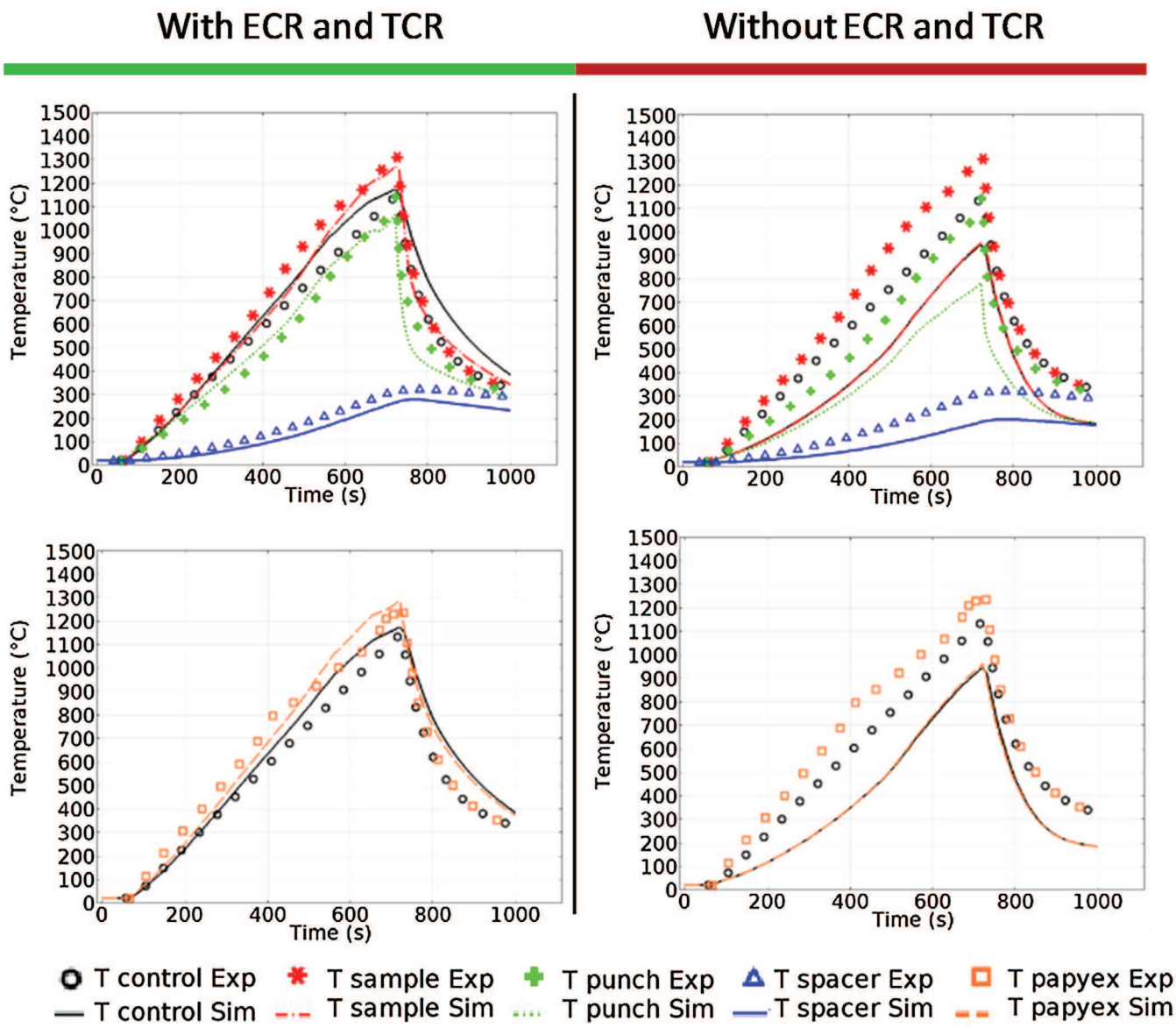

Fig. 14. Experimental/simulated temperatures for the independent verification test with and without contact resistances.

pressure (Fig. 16). For each pressure, 6 measurements are reported. A sharp decrease of the global TCR can be noticed at low pressure between 0.5 and 2 MPa, for the two interfaces (Fig. 16a and b). After 2 MPa the TCR values for the two interfaces reach almost the same value, around 4E–5 Km^2/W, and continue to decrease slowly with the pressure.

3.5. *Ex situ/in situ discussions*

The main ECR and TCR order of magnitudes in the literature and the present study are reported in Table 4. When needed, the ECR and TCR have been calculated using the tools dimensions and temperatures data. The order of magnitude of the ECR in horizontal/vertical directions and horizontal TCR is in accordance with [6,10–12,16,17,22,24,25]. However the vertical TCR is a bit higher in our case (5.00E-03 m^2 K/W instead of about 5 E-04 m^2 K/W for [10,11,22,25] and 1.14E-03 m^2 K/W for [16]). The vertical TCR seem to be underestimate in the others authors calibrations.

The ex situ vs in situ ECR & TCR comparison can be made on the contacts where the papyex is employed. The contacts considered are located at the punch/sample, sample/die and the punch/die

Table 4
Order of magnitude of the ECR and TCR of the literature compared to the present results at 1000 °C in horizontal (H) and vertical (V) directions.

	ECR ($\Omega\ m^2$)	TCR (m^2 K/W)
Zavaliangos et al. [10] Maizza et al. [11] Giuntini et al. [22]	H 8.00E-08 V 1.33E-07	H 4.17E-04 V 7.58E-04
Matsugi et al. [6]	H 0 V 5.00E-07	H 5.56E-06 V 6.62E-06
Vanmeensel et al. [23]	H 1.26E-07 V 2.76E-06	–
Wei et al. [17]	H 1.39E-08 V 1.08E-06	–
Cincotti et al. [24]	1.47E-07	3.50E-06
Muñoz et al. [25]	H 2.00E-08 V 1.20E-07	H 6.67E-05 V 4.00E-04
Arnaud et al. [16] (interface with graphite spray)	H 1.67E-08 V 6.72E-08	H 2.00E-04 V 1.14E-03
Present study: in situ method	H 1.00E-08 V 8.00E-08	H 5.00E-04 V 5.00E-03
Present study: ex situ method (8 MPa at room temperature)	1.50E-07	5.00E-05

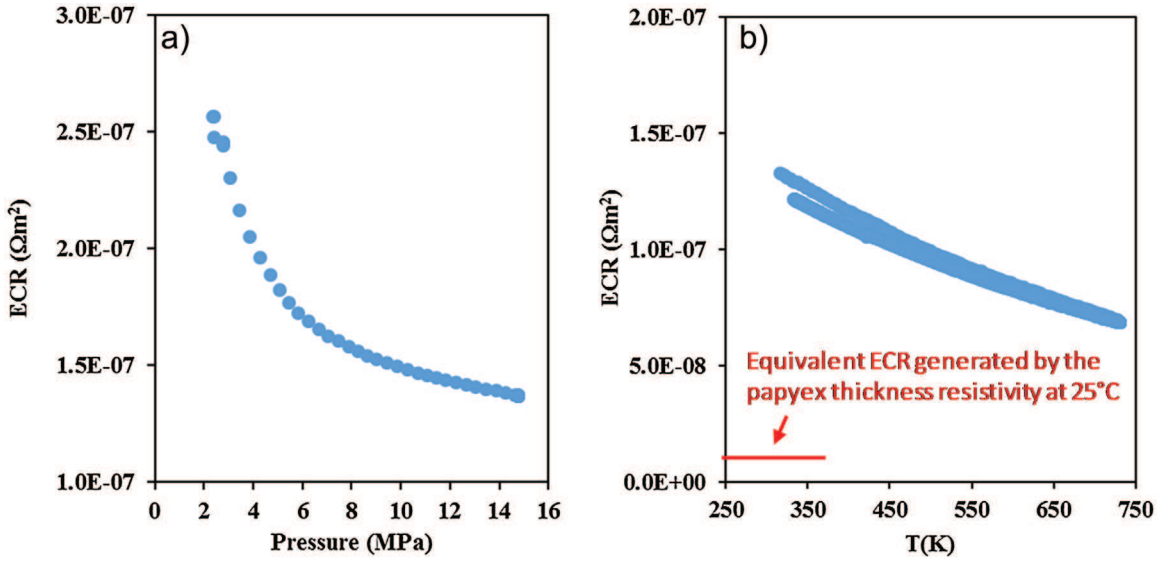

Fig. 15. Ex situ measurements of graphite-papyex-graphite ECR (electrical contact resistances) a) function of pressure (T = 295 K), b) function of temperature (P = 15 MPa).

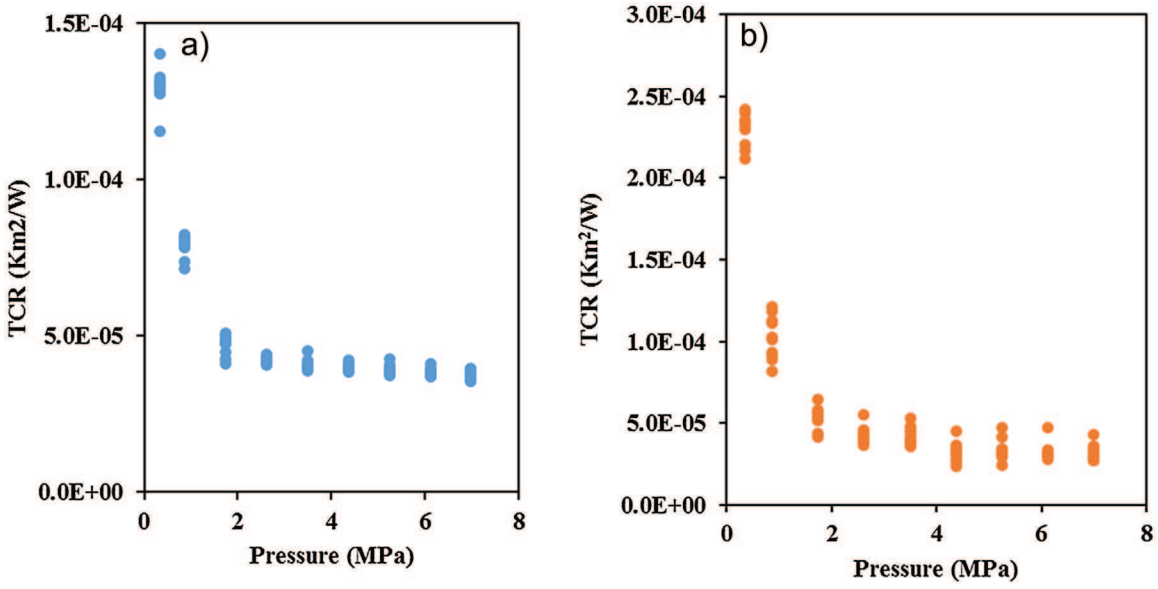

Fig. 16. Ex situ measurements of TCR (thermal contact resistances) function of pressure (T=250 °C): a) $TCR_{graphite\text{-}papyex\text{-}graphite}$, and b) $TCR_{alumina\text{-}papyex\text{-}graphite}$.

interfaces. The punch/sample contact is subject to a pressure of 50 MPa. The sample/die contact is subject to a pressure induced by the creep deformations of the porous matter and by the difference between the thermal dilation between the sample and the die. The alumina/papyex/graphite contacts (sample/die and sample/punch interfaces) are analyzed first. The ex situ measurements show a relatively stable value around 4E–5 Km^2/W of TCR above 2 MPa of applied pressure while the calibrated in situ values are between 1E-5 and 1E–4 Km^2/W. The ex situ TCR value is then located roughly in the middle of the in situ range.

The punch/die is a contact for which it is difficult to determine the level of pressure but it is reasonably assumed to be very low. Furthermore, in the case where an electric insulator is densified, like alumina here, the totality of the current is forced across this contact. The calibrated TCR (in situ) are between 1E-4 and 4E–2 Km^2/W, the ex situ measurements give values decreasing asymptotically with pressure to a value of 4E–5 Km^2/W above 2 MPa while a drastic increase (nearly exponential) of the TCR is observed below 2 MPa up to values of 1.5E–4 Km^2/W in the pressure range explored. This result suggests a very low contact pressure for the low temperature regime and a contact pressure of around 1 MPa for the high temperature regime (see Fig. 16a). For the SPS experiment point of view, a high TCR is mandatory to account for the temperatures observed between the punch and the die (see Fig. 9 and Fig. 10). Considering the 0.2 mm gap inside the punch/die interface where the papyex, a compressible material, is located, a low punch/die pressure is not surprising. Concerning the electrical aspect of the contact, the calibrated ECR (in situ) is evaluated at around 3.2E–7 $\Omega\,m^2$ for the low temperature regime and 1E–7 $\Omega\,m^2$ for the high temperatures regime. The ex situ ECR are from 2.5E-7 to 5E–8 $\Omega\,m^2$. The corresponding contact pressure is lower than 1 MPa for the low temperatures and 15 MPa for the high temperatures (see Fig. 15). Then, for the punch/die interface, the quality of the contact seems better for the electrical part compared to the thermal part. This difference suggests that the electric

current flow across the contact interface is facilitating the high temperatures irrespective of the quality of the contact interface.

4. Conclusion

The behavior of the ECR and TCR of the different contacts present in several SPS column types was investigated by in situ calibration and ex situ measurements. The in situ study revealed the preponderant role and the diversity of the ECR and TCR in the overall temperature field. The ECR are responsible for a general warming of the entire SPS column while the TCR explains the temperature gradients. Particular attention is paid to the lateral punch/die interface where a high value of the TCR was found. This TCR is responsible for the large temperature difference observed between the punch, the sample and the die. In order to extend the validity domain of the calibrated ECR and TCR, calibrations were made with three different sample diameters at a constant applied pressure of 50 MPa. The extended model obtained was tested on an independent 15 mm punch diameter and showed close simulated and measured results.

The ex situ measurements indicated stable values of the TCR after 2 MPa of about 4E–5 $K m^2/W$ and ECR values of about 1.4E–7 Ωm^2 for all the central contacts using papyex. The comparison between ex situ and in situ values determined for the punch/die interface shows higher in situ TCR values leading to a probable very low contact pressure and to a comparable order of magnitude for the ECR. The fact that for the same contact conditions, the ECR corresponds to higher contact quality than the TCR (as regards the ex situ measurements) suggests a mechanism that facilitates the interface electric current flow at the high temperatures such as possible combined actions of field and/or thermionic electron emission or other phenomena.

Acknowledgments

The authors are grateful to the National Research Agency for the financial support. REF ANR: ANR-09-MAPR-0007-MAPR. Impulse.

References

[1] Z.A. Munir, U. Anselmi-Tamburini, M. Ohyanagi, The effect of electric field and pressure on the synthesis and consolidation of materials: a review of the spark plasma sintering method, J. Mater. Sci. 41 (2006) 763–777, http://dx.doi.org/10.1007/s10853-006-6555-2.

[2] R. Orrù, R. Licheri, A.M. Locci, A. Cincotti, G. Cao, Consolidation/synthesis of materials by electric current activated/assisted sintering, Mater. Sci. Eng. R: Rep. 63 (2009) 127–287, http://dx.doi.org/10.1016/j.mser.2008.09.003.

[3] S. Grasso, Y. Sakka, G. Maizza, Electric current activated/assisted sintering (ECAS): a review of patents 1906–2008, Sci. Technol. Adv. Mater. 10 (2009) 053001, http://dx.doi.org/10.1088/1468-6996/10/5/053001.

[4] O. Guillon, J. Gonzalez-Julian, B. Dargatz, T. Kessel, G. Schierning, J. Räthel, et al., Field-assisted sintering technology/spark plasma sintering: mechanisms, materials, and technology developments, Adv. Eng. Mater. 16 (2014) 830–849, http://dx.doi.org/10.1002/adem.201300409.

[5] B.-N. Kim, K. Hiraga, K. Morita, H. Yoshida, Effects of heating rate on microstructure and transparency of spark-plasma-sintered alumina, J. Eur. Ceram. Soc. 29 (2009) 323–327, http://dx.doi.org/10.1016/j.jeurceramsoc.2008.03.015.

[6] K. Matsugi, H. Kuramoto, T. Hatayama, O. Yanagisawa, Temperature distribution at steady state under constant current discharge in spark sintering process of Ti and Al2O3 powders, J. Mater. Process. Technol. 134 (2003) 225–232, http://dx.doi.org/10.1016/s0924-0136(02)01039-7.

[7] G. Molénat, L. Durand, J. Galy, A. Couret, Temperature control in spark plasma sintering: an FEM approach, J. Metall. 2010 (2010) 1–9, http://dx.doi.org/10.1155/2010/145431.

[8] A. Pavia, L. Durand, F. Ajustron, V. Bley, G. Chevallier, A. Peigney, et al., Electro-thermal measurements and finite element method simulations of a spark plasma sintering device, J. Mater. Process. Technol. 213 (2013) 1327–1336, http://dx.doi.org/10.1016/j.jmatprotec.2013.02.003.

[9] J.B. Allen, C. Walter, Numerical simulation of the temperature and stress field evolution applied to the field assisted sintering technique, ISRN Mater. Sci. 2012 (2012) 1–9, http://dx.doi.org/10.5402/2012/698158.

[10] A. Zavaliangos, J. Zhang, M. Krammer, J.R. Groza, Temperature evolution during field activated sintering, Mater. Sci. Eng. A 379 (2004) 218–228, http://dx.doi.org/10.1016/j.msea.2004.01.052.

[11] G. Maizza, S. Grasso, Y. Sakka, Moving finite-element mesh model for aiding spark plasma sintering in current control mode of pure ultrafine WC powder, J. Mater. Sci. 44 (2009) 1219–1236, http://dx.doi.org/10.1007/s10853-008-3179-8.

[12] K. Vanmeensel, A. Laptev, O. Van der Biest, J. Vleugels, Field assisted sintering of electro-conductive ZrO2-based composites, J. Eur. Ceram. Soc. 27 (2007) 979–985, http://dx.doi.org/10.1016/j.jeurceramsoc.2006.04.142.

[13] C. Maniere, A. Pavia, L. Durand, G. Chevallier, V. Bley, K. Afanga, et al., Pulse analysis and electric contact measurements in spark plasma sintering, Electr. Power Syst. Res. 127 (2015) 307–313, http://dx.doi.org/10.1016/j.epsr.2015.06.009.

[14] U. Anselmi-Tamburini, S. Gennari, J.E. Garay, Z.A. Munir, Fundamental investigations on the spark plasma sintering/synthesis process, Mater. Sci. Eng. A 394 (2005) 139–148, http://dx.doi.org/10.1016/j.msea.2004.11.019.

[15] C. Manière, A. Pavia, L. Durand, G. Chevallier, K. Afanga, C. Estournès, Finite-element modeling of the electro-thermal contacts in the spark plasma sintering process, J. Eur. Ceram. Soc. (2015), http://dx.doi.org/10.1016/j.jeurceramsoc.2015.10.033.

[16] C. Arnaud, C. Manière, G. Chevallier, C. Estournès, R. Mainguy, F. Lecouturier, et al., Dog-bone copper specimens prepared by one-step spark plasma sintering, J. Mater. Sci. 50 (2015) 7364–7373, http://dx.doi.org/10.1007/s10853-015-9293-5.

[17] X. Wei, D. Giuntini, A.L. Maximenko, C.D. Haines, E.A. Olevsky, Experimental investigation of electric contact resistance in spark plasma sintering tooling setup, J. Am. Ceram. Soc. 98 (2015) 3553–3560, http://dx.doi.org/10.1111/jace.13621.

[18] E.A. Olevsky, C. Garcia-Cardona, W.L. Bradbury, C.D. Haines, D.G. Martin, D. Kapoor, Fundamental aspects of spark plasma sintering: II. Finite element analysis of scalability, J. Am. Ceram. Soc. 95 (2012) 2414–2422, http://dx.doi.org/10.1111/j.1551-2916.2012.05096.x.

[19] C. Manière, L. Durand, A. Weibel, C. Estournès, Spark-plasma-sintering and finite element method: from the identification of the sintering parameters of a submicronic α-alumina powder to the development of complex shapes, Acta Mater. 102 (2016) 169–175, http://dx.doi.org/10.1016/j.actamat.2015.09.003.

[20] P. Rogeon, P. Carre, J. Costa, G. Sibilia, G. Saindrenan, Characterization of electrical contact conditions in spot welding assemblies, J. Mater. Process. Technol. 195 (2008) 117–124.

[21] P. Carre, P. Rogeon, E. Dupe, G. Deruet, G. Sibilia, Détermination des paramètres interfaciaux pour la modélisation du soudage par points de tôles d'acier revêtues, J. Int. de Therm. (2005) 287–290 (Tanger, Maroc, 15–17 Novembre).

[22] D. Giuntini, E. Olevsky, C. Garcia-Cardona, A. Maximenko, M. Yurlova, C. Haines, D. Martin, D. Kapoor, Localized overheating phenomena and optimization of spark-plasma sintering tooling design, Materials 6 (2013) 2612–2632, http://dx.doi.org/10.3390/ma6072612.

[23] K. Vanmeensel, A. Laptev, J. Hennicke, J. Vleugels, O. Vanderbiest, Modelling of the temperature distribution during field assisted sintering, Acta Mater. 53 (2005) 4379–4388, http://dx.doi.org/10.1016/j.actamat.2005.05.042.

[24] A. Cincotti, A.M. Locci, R. Orr&#x00F9, G. Cao, Modeling of SPS apparatus: temperature, current and strain distribution with no powders, AIChE J. 53 (2007) 703–719, http://dx.doi.org/10.1002/aic.11102.

[25] S. Muñoz, U. Anselmi-Tamburini, Temperature and stress fields evolution during spark plasma sintering processes, J. Mater. Sci. 45 (2010) 6528–6539, http://dx.doi.org/10.1007/s10853-010-4742-7.